inorganics

MDPI

Article

^{96}Zr Tracer Diffusion in $AZro_3$ (A = Ca, Sr, Ba)

Rokas Sažinas [1,2], Isao Sakaguchi [2], Mari-Ann Einarsrud [1] and Tor Grande [1,*]

[1] Department of Materials Science and Engineering, NTNU Norwegian University of Science and Technology, NO-7491 Trondheim, Norway; rokas.sazinas@gmail.com (R.S.); mari-ann.einarsrud@ntnu.no (M.-A.E.)

[2] Research Center for Functional Materials, National Institute for Materials Science, Tsukuba 305-0044, Japan; sakaguchi.isao@nims.go.jp

* Correspondence: grande@ntnu.no; Tel.: +47-7359-4084

Received: 30 November 2017; Accepted: 9 January 2018; Published: 15 January 2018

Abstract: Cation tracer diffusion in polycrystalline $AZrO_3$ (A = Ca, Sr, Ba) perovskites was studied at 1300–1500 °C in air using the stable isotope ^{96}Zr. Thin films of $^{96}ZrO_2$ were deposited on polished ceramic pellets by drop casting of an aqueous precursor solution containing the tracer. The pellets were subjected to thermal annealing, and the isotope depth profiles were measured by secondary ion mass spectrometry. Two distinct regions with different slopes in the profiles enabled to assess separately the lattice and grain boundary diffusion coefficients using Fick's second law and Whipple–Le Clair's equation. The cation diffusion along grain boundaries was 4–5 orders of magnitude faster than the corresponding lattice diffusion. The magnitude of the diffusivity of Zr^{4+} was observed to increase with decreasing size of the A-cation in $AZrO_3$, while the activation energy for the diffusion was comparable 435 ± 67, 505 ± 56, and 445 ± 45 and kJ·mol^{-1} for $BaZrO_3$, $SrZrO_3$, and $CaZrO_3$, respectively. Several diffusion mechanisms for Zr^{4+} were considered, including paths via Zr- and A-site vacancies. The Zr^{4+} diffusion coefficients reported here were compared to previous data reported on B-site diffusion in perovskites, and Zr^{4+} diffusion in fluorite-type compounds.

Keywords: cation diffusion; perovskite oxides; Zr tracer diffusion

1. Introduction

Mixed metal oxides $AZrO_3$ (A = Ba, Sr, Ca) with perovskite structure have received considerable attention as their properties may be tailored for specific applications by doping at the A or B cation sites. $AZrO_3$ perovskite materials are attractive due to their high proton conductivity, with potential applications in protonic ceramic fuel cells (PCFC), electrolyzers, gas sensors, and hydrogen membrane technology [1–7]. The majority of studies on $AZrO_3$ proton conductors have focused on the transport properties, but a recent study has also addressed the mobility of cations in the $BaZrO_3$ (BZ)-materials, revealing the challenges with solid state sintering of the ceramics and chemical instability in CO_2 at elevated temperature [8].

$AZrO_3$ materials belong to the family of $A^{II}B^{IV}O_3$ perovskites among which cation diffusion has only been investigated in $ATiO_3$ (A = Ba, Sr), and recently in BZ and $BaMO_3$ (M = Ti, Zr, Ce) [9–18]. Systematic studies of factors influencing the cation diffusion, such as A- and B-site cation size, unit cell volume, and concentration of point defects in the materials, are still lacking. Recently, it has been shown that A-site diffusion is faster than B-site diffusion in BZ [17]. Knowledge of the difference in the cation mobility at the different cation sub-lattices is vital for the understanding of the long-term stability of the materials in chemical potential gradients [19]. Moreover, cation diffusion is also relevant for the reactivity of materials with e.g., CO_2, as recently shown for BZ-materials [20]. Cation diffusion in oxides is important for the processing of dense ceramics, and $AZrO_3$ materials are known for their high melting temperatures and slow sintering rates [21–23]. Consequently, the slow migration of

the backbone-forming Zr^{4+}-cations in the perovskites is most likely the reason for the required high sintering temperature for BZ-based ceramics [17].

Recently, we have reported on a systematic investigation of Ba diffusion in $BaMO_3$ (M = Ti, Zr, Ce) [18], and here, we present a corresponding systematic investigation of ^{96}Zr cation tracer diffusion in polycrystalline $AZrO_3$ (A = Ba, Sr, Ca), measured by secondary ion mass spectrometry (SIMS). The experimental data were obtained by annealing dense $AZrO_3$ ceramics coated with thin films of $^{96}ZrO_2$ in the temperature range 1300–1500 °C. The ^{96}Zr SIMS depth profiles enabled us to determine lattice and grain boundary diffusion coefficients, and the corresponding activation energies. The cation diffusion data were discussed with respect to the dependence of the Zr^{4+} mobility, with respect to the size of the A-cation in the perovskite lattice and the crystal symmetry. Finally, the diffusivity of Zr^{4+} in $AZrO_3$ was compared to the B-site mobility in perovskite oxides in general, and the corresponding diffusion of Zr^{4+} in ZrO_2-based fluorite materials.

2. Results

X-ray diffraction (XRD) patterns of the three materials CZ ($CaZrO_3$), SZ ($SrZrO_3$), and BZ ($BaZrO_3$) could be indexed to single-phase perovskite materials (see Figure S1). The unit cell parameters obtained by Rietveld refinement of the diffraction patterns are summarized in Table 1 and in Table S1. The sintered ceramics resulted in phase pure CZ, SZ, and BZ materials with relative density higher than 97% of the theoretical density. Scanning electron microscopy (SEM) micrographs of the three ceramics after thermal etching are shown in Figure 1. The grain size of the three materials were 10.5 ± 0.2, 5.2 ± 0.1, and 1.1 ± 0.1 µm, respectively. The grain size and relative density of the materials are summarized in Table 1.

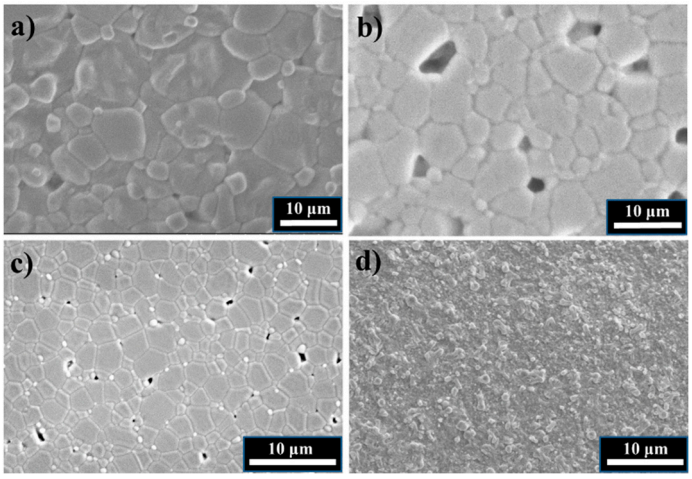

Figure 1. The microstructure of the sintered and thermally etched (**a**) CZ; (**b**) SZ; (**c**) BZ ceramics; and (**d**) $^{96}ZrO_2$ layer deposited on the surface of ceramics. Pores in (**b**) are due to grain pull out during polishing.

Table 1. Crystal structure, unit cell parameters, grain size, and relative density of the three materials BZ, SZ, and CZ.

Material	Crystal Structure	Unit Cell Parameters (Å)	Grain Size (µm)	Relative Density (%)
$BaZrO_3$	Cubic $Pm\bar{3}m$	$a = 4.193$	0.1	97 ± 1
$SrZrO_3$	Orthorhombic *Pbnm*	$a = 5.797$ $b = 5.824$ $c = 8.209$	5.2 ± 0.1	96 ± 2
$CaZrO_3$	Orthorhombic *Pnma*	$a = 5.763$ $b = 8.023$ $c = 5.596$	10.5 ± 0.2	98 ± 1

SEM micrograph of the films of monoclinic $^{96}ZrO_2$ on one of the materials is shown in Figure 1d. The films were homogeneous and crack-free, and about 1–2 μm thick, with good attachment to the surface of the pellets of CZ, SZ, and BZ. The thickness of the $^{96}ZrO_2$ layer was controlled by the total amount of tracer in the precursor solution deposited on each pellet. The phase purity of the films was confirmed by XRD (not shown), and the chemical composition was confirmed by SEM/energy dispersive spectroscopy.

The depth profile of ^{96}Zr diffusion in SZ after annealing at 1450 °C for 4 h are given in Figure 2. The graph shows the logarithmic normalized intensity of the secondary molecular ion $^{96}ZrO^-$ as a function of the depth. The depth profile demonstrates the changes of the tracer concentration from the $^{96}ZrO_2$/SZ interface towards the bulk. The concentration of the tracer became close to constant at a larger depth, corresponding to the natural abundance of ^{96}Zr. Two distinct regions for lattice and grain boundary diffusion were identified as regions A and B in Figure 2, respectively. The parts of the ^{96}Zr depth profiles related to lattice and grain boundary diffusion are included in the insets of Figure 2. The data is plotted as a function of x^2 and $x^{6/5}$ in the two regions, and the linear fits to the data according to Equations (5) and (6) (see Section 4) are shown by the red curves. Depth profile, such as the one shown in Figure 2, and corresponding processing of the data were obtained for all the three materials at all the conditions for the tracer annealing.

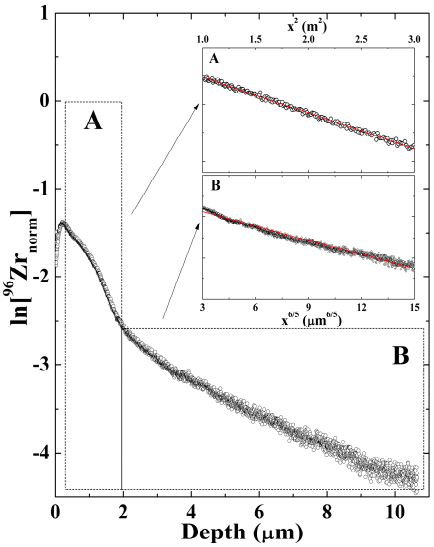

Figure 2. SIMS depth profile for ^{96}Zr diffusion in polycrystalline SZ annealed at 1450 °C for 4 h. The insets represent the two regions, A and B, modified for the fitting of lattice and grain boundary diffusion coefficients, respectively, together with the fit to the data (red lines).

The critical parameters, α and β, which represent the ratio of the bulk and grain-boundary diffusion to the effective diffusion coefficient, were calculated from the lattice and grain boundary diffusion coefficients, D_L and D_{GB} [24]. α and β are defined as the partial contribution of the lattice and grain boundary diffusion coefficient, respectively, to the effective diffusion coefficient. The calculated α values were in the range 0.01–0.03, and corresponding β values exceeded 50, demonstrating that the condition to determine D_{GB} by Equation (6) was fulfilled (β > 10) [24].

The logarithmic tracer diffusion coefficients of ^{96}Zr in $AZrO_3$ (A = Ca, Sr, Ba) as a function of reciprocal temperature, are summarized in Figure 3. The diffusion coefficients follow an Arrhenius behavior. The magnitude of the lattice diffusion coefficient increased in the order $BaZrO_3$, $SrZrO_3$, and $CaZrO_3$, reflecting the decreasing size of the A-cation. The activation energy for lattice diffusion determined by the linear fit to the data is summarized in Table 2. The pre-exponential factor in the Arrhenius expression varied in the range 0.4–220 for the lattice diffusion, see Table 2. The grain boundary diffusion coefficients were 4–5 orders of magnitude higher than the corresponding data

for the lattice diffusion. The activation energy for cation transport along grain boundaries is 20–120 kJ·mol^{-1} lower compared to the corresponding activation energy for lattice diffusion (Table 2).

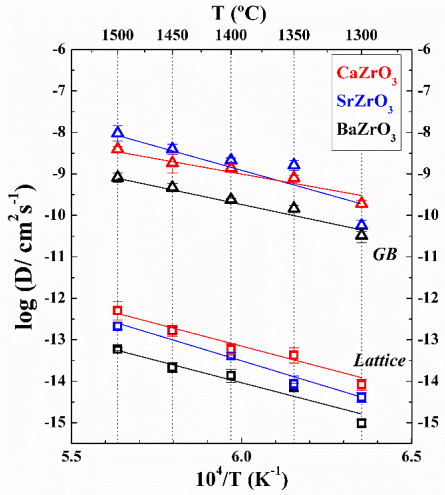

Figure 3. Arrhenius plot of the ^{96}Zr diffusion coefficients in $AZrO_3$ (A = Ca, Sr, Ba). The uncertainty for each data point is the standard deviation obtained by the fitting of the depth profiles.

Table 2. The pre-exponential factor and activation energy for ^{96}Zr lattice and grain boundary diffusion in $AZrO_3$ perovskites determined by the fit of the tracer diffusion data to the Arrhenius equation.

Material	D_o (cm^2/s)	$E_{a,\ \text{lattice}}$ (kJ/mol)	$E_{a,\ \text{GB}}$ (kJ/mol)
$BaZrO_3$	0.4 ± 0.1	435 ± 67	356 ± 40
$SrZrO_3$	220 ± 90	505 ± 56	523 ± 134
$CaZrO_3$	6.3 ± 1.4	445 ± 45	322 ± 46

The activation energy for ^{96}Zr lattice diffusion is plotted against the unit cell volume per formula unit (f.u.) of the $AZrO_3$ perovskites in Figure 4. The activation energy is decreasing with increasing unit cell volume per formula unit for the two cubic perovskites BZ and SZ (cubic at the measurement temperature), while the orthorhombic CZ has an activation energy intermediate between the two others.

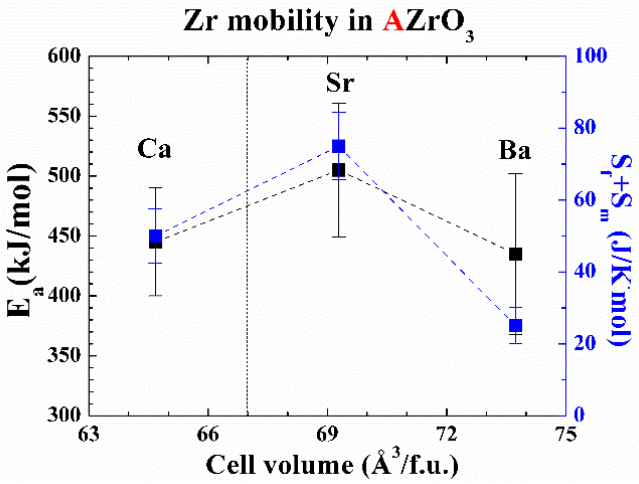

Figure 4. The dependence of the activation energy for ^{96}Zr lattice diffusion in $AZrO_3$ perovskites and corresponding activation entropy of formation and migration on the unit cell volume per formula unit (f.u.).

3. Discussion

The possible pathways for Zr^{4+} migration through the cubic perovskite $BaZrO_3$ lattice are visualized in Figure 5. The path A illustrates Zr^{4+} diffusion via a Ba-vacancy, while path C shows Zr^{4+} diffusion via a Zr-vacancy. The most likely combination of Zr^{4+} migration involving both site vacancies is shown in path B in Figure 5. Recently, we have shown that the diffusion pathway for Zr^{4+} via Ba-vacancies is most likely in BZ [17], and we propose that this diffusion mechanism can also be expected for cubic SZ also supported by previous studies [15,25].

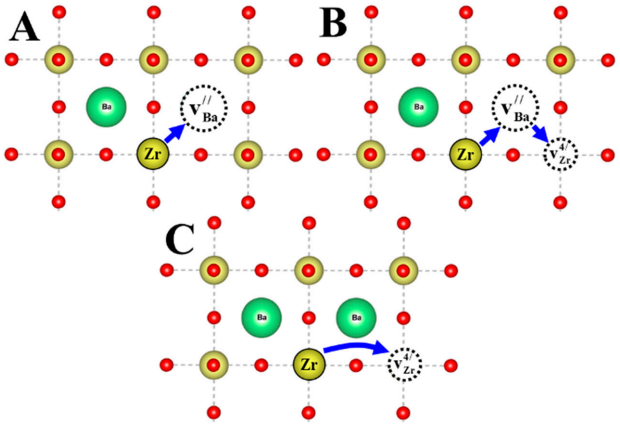

Figure 5. A schematic of diffusion pathways for Zr^{4+} cations in non-stoichiometric $BaZrO_3$: (**A**) via Ba-vacancy; (**B**) via both Ba- and Zr-vacancies; (**C**) via Zr-vacancy. Zr yellow, Ba green, O red. Relaxation of the crystal structure around the vacancies are not included in the illustration for simplicity.

The crystal structure of CZ is orthorhombic compared to the cubic structure of BZ and SZ at 1300–1500 °C. The phase transition to cubic SZ has been reported at 1087 °C [26], while CZ is orthorhombic up to 2000 °C [27]. Thus, the diffusion mechanism for CZ cannot be argued for based on diffusion in cubic BZ or SZ. The intermediate local configurations along the diffusion path together with activation energy are different, due to the orthorhombic symmetry. The orthorhombic distortion of CZ crystal structure is significant in the temperature region of the present measurements [28]. The activation energy for diffusion for CZ deviates from the trend from BZ to SZ (Figure 4), which support a modified diffusion path for Zr in CZ relative to the one proposed for the two cubic compounds.

Ionic diffusion in solids depends on point defects in the lattice. The main contribution to point defects in the compounds is the frozen-in point defects after processing at higher temperature, and the change in the point defect concentration during tracer anneal at considerably lower temperature is minor [17,18,29]. The possible point defects in $AZrO_3$ are the oxygen vacancies ($v_O^{\bullet\bullet}$), A-site vacancies (v_A''), Zr vacancies ($v_{Zr}^{4\prime}$) [30], Zr anti-site ($Zr_A^{\bullet\bullet}$) [31], A-interstitials (A_i^x), and Zr interstitials (Zr_i^x). The metal interstitial defects are not energetically favored, and less likely to be present [30,32]. Thus, the main point defect equilibria relevant for Zr^{4+} diffusion in $AZrO_3$ perovskites can be described by point defect reactions (1) and (2) [30,32]

$$\text{nill} \rightarrow v_A'' + v_{Zr}^{4\prime} + 3v_O^{\bullet\bullet} \quad (1)$$

$$A_A^x + O_O^x \rightarrow v_A'' + v_O^{\bullet\bullet} + AO \quad (2)$$

where Equation (1) corresponds to the full Schottky equilibrium, and Equation (2) to the A-site partly Schottky equilibrium. The energy of formation for these point defect equilibria, available in the literature for the three materials, are summarized in Table 3. The formation of A-site partly Schottky-type defects is significantly lower in energy than for the corresponding B-site. According to Table 3, the formation energies for full Schottky-type defects, reaction (1), are decreasing in the order SZ, BZ, and CZ [29,31], while the energies of formation for the AO partly Schottky-type defects decrease

in the order BZ, SZ, and CZ. Higher energy of formation implies lower concentration of the frozen-in defects, and slower cation diffusivity is inferred. It is, however, important to note that the formation and loss of volatile BaO at high temperatures has been detected in BZ-materials [8,33], while evidence for the loss of SrO and CaO, from SZ and CZ, has not been reported.

Table 3. The energy of formation of point defects in BZ, SZ, and CZ according to Equation (5) and (6), taken from the literature.

Material	Cation Sublattice	Cation Size [34] (Å)	Partly Schottky Defect (eV/Defect)	Schottky Defect (eV/Defect)	Reference
$BaZrO_3$	Zr Ba	0.72 1.61	3.75 2.80	3.20	[30]
$SrZrO_3$	Zr Sr	0.72 1.44	4.45 2.68	3.51	[32]
$CaZrO_3$	Zr Ca	0.72 1.34	3.09 1.26	2.22	

In general, the diffusion coefficient for a mechanism involving ionic jumps to a vacant adjacent site is expressed by an Arrhenius expression [35]:

$$D = D_0 \exp\left(-\frac{E_a}{RT}\right) = D_0 \exp\left(-\frac{\Delta H_f + \Delta H_m}{RT}\right) \quad (3)$$

where, E_a is the activation energy of diffusion, ΔH_f is the enthalpy of formation of the vacancy, ΔH_m is enthalpy of migration of the diffusing species, R is the gas constant, T is temperature, and D_0 is the pre-exponential factor. The pre-exponential factor is a temperature-independent constant experimentally determined from the fit to the Arrhenius equation and can be expanded as Equation (4) [36]:

$$D_0 = \lambda^2 \eta \exp\left(\frac{S_f + S_m}{k_B}\right) \quad (4)$$

where, λ is the jump distance, η is the vibration frequency, and S_f and S_m are the entropy of formation and migration of cation vacancies, respectively.

We have recently argued that the activation energy barrier for Ba^{2+} diffusion in BZ is mainly dominated by the enthalpy of migration [18]. Including the fact that $AZrO_3$ materials are refractory in terms of sintering, and the defect chemistry is dominated by frozen-in point defects especially on the A-site after sintering, the contribution of the enthalpy of formation to the activation energy is assumed negligible at 1300–1500 °C. The experimental activation energies for Zr^{4+} diffusion in all three materials given in Figure 4 imply that increased A-cation size energetically favors Zr^{4+} mobility in BZ compared to SZ. The reasons could be attributed to more space for the migration, and lower Coulomb's repulsion between the two cations A–A or A–B (see Figure 5). A similar trend has been previously observed for Ba^{2+} diffusion in cubic Ba-based perovskites [18]. The activation energy for Zr^{4+} diffusion in CZ is the lowest, meaning that the environment of the intermediate diffusion configurations is different compared to cubic perovskites. We proposed that the low energy of formation of the partly and full Schottky-type defects for CZ, compared to the two other compounds (Table 3), and corresponding higher frozen-in defect concentration, favor the Zr^{4+} diffusivity in CZ.

The cation transport along grain boundaries in all three materials is stimulated by the lower activation energy compared to activation energy for lattice diffusion. One could argue that the mobility along grain boundaries is facilitated by the higher concentration of cation vacancies at grain boundaries, more space available for the diffusion, and reduced Coulomb's repulsion due to longer distances between the ions at the grain boundary.

The Arrhenius-type relationship of for Zr^{4+} diffusion in $AZrO_3$ perovskites encouraged us to assess the value of pre-exponential factor, D_0, and calculate the entropy of the diffusion process

according to Equation (4). Referring to previous studies, the pre-exponential factor includes the entropy term, which consists of entropy of formation and migration for cation vacancies [18,36]. Based on the consideration of the activation enthalpy of migration, we also propose that the entropy term is dominated by the entropy of migration [37]. In the comparison of all three materials, it can be seen that the dependence of migration entropy on the unit cell volume per formula unit is similar to the corresponding enthalpy of migration (Figure 4), and is decreasing in the order SZ, CZ, and BZ. The lowest entropy value is estimated for BZ, meaning that the disorder due to migration is lower, and correspondingly, the Zr^{4+} mobility in BZ will be less favored compared to the other materials.

Figure 6 compares the Zr^{4+} diffusivity in $AZrO_3$ to the B-site diffusivities in perovskites reported in the literature. The B-site diffusion in $AZrO_3$ is slower than in most of the $A^{III}B^{III}O_3$ perovskites, with tolerance factor less than 1, due to increased charge of Zr^{4+} [38]. Unfortunately, the dominating diffusion mechanisms are usually not known for most of the data for $A^{III}B^{III}O_3$ perovskites, which challenge the comparison of data in the literature. The B-site diffusion in $AZrO_3$ is favored by higher activation energy than in $A^{III}B^{III}O_3$ perovskites, revealing that the increased charge and tolerance factor reduces the B-site mobility in $AZrO_3$. One could envisage that the lower tolerance factor facilitates cation diffusion as in $A^{III}B^{III}O_3$ compared to $A^{II}B^{IV}O_3$ [17]. Correspondingly, the current diffusion data in CZ gives additional information that the decrease in the tolerance factor with corresponding distortion favors Zr^{4+} mobility, shifting it closer to the B-site mobility in $A^{III}B^{III}O_3$.

The diffusion coefficients of fluorite-type materials are summarized in Figure 7, and compared to experimental Zr^{4+} diffusion coefficients from the current study. It can be seen that the mobility of Zr^{4+} in $AZrO_3$ perovskites is of the same order of magnitude as in fluorite-type oxides, such as YSZ. Figure 7 implies that Zr^{4+} in the $AZrO_3$ materials is as slow as in ZrO_2-based oxides, with fluorite structure revealing the low mobility of B-site in the cubic and orthorhombic $AZrO_3$ perovskites.

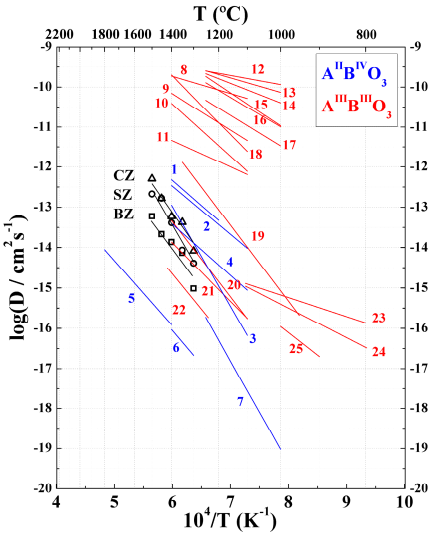

Figure 6. Zr diffusivity in $AZrO_3$ compared for $A^{II}B^{IV}O_3$ and $A^{III}B^{III}O_3$ perovskites. Abbreviations: p—polycrystalline; sc—single crystal; c—cubic; b—bulk; gb—grain boundaries. (1) Ho in p $BaTiO_3$ gb [11]; (2) Ho in p $BaTiO_3$ b [11]; (3) Ni in p $Ba(Ho,Ti)O_3$ [10]; (4) Ni in sc $BaTiO_3$ [10]; (5) Ni in p $BaTiO_3$ [10]; (6) Si in $MgSiO_3$ [39]; (7) ^{49}Ti in sc $(La,Sr)TiO_3$ [25]; (8) Zr in sc $BaTiO_3$ [12]; (9) ^{141}Pr in $LaFeO_3$ gb [40]; (10) 141Pr in LaCoO3 gb [40]; (11) Co in $LaCoO_3$ gb [41]; (12) Cr in $LaMnO_3$ [42]; (13) Mn in $LaCoO_3$ [43]; (14) Co in $LaCoO_3$ b [41]; (15) ^{141}Pr in $LaMnO_3$ [40]; (16) Co in $GdCoO_3$ [44]; (17) Co in $EuCoO_3$ [44]; (18) Co in $SmCoO_3$ [44]; (19) Co in $NdCoO_3$ [44]; (20) Co in $PrCoO_3$ [44]; (21) ^{50}Cr in $(La,Ca)CrO_3$ gb [45]; (22) Co in $LaCoO_3$ [44]; (23) Mn in $LaMnO_3$ b [42]; (24) Mn in $LaMnO_3$ gb [42]; (25) Fe in $LaFeO_3$ gb [46]; (26) Fe in $LaFeO_3$ b [46]; (27) ^{141}Pr in $LaCoO_3$ b [40]; (28) ^{141}Pr in $LaFeO_3$ b [40]; (29) Fe in $NdFeO_3$ p [47]; (30) Fe in $(La,Sr)CoO_3$ [48]; (31) Fe in $(La,Sr)FeO_3$ [48]; (32) ^{50}Cr in $(La,Ca)CrO_3$ b [45].

The low mobility of Zr^{4+} in the current materials, evident by the comparison in Figure 7, is beneficial with respect to the chemical stability in potential gradients, but will shift the sintering temperature of the materials to high temperatures. High sintering temperatures are needed to obtain high density $AZrO_3$ materials, reflecting that the slow diffusion of Zr^{4+} is rate limiting for the sintering [8].

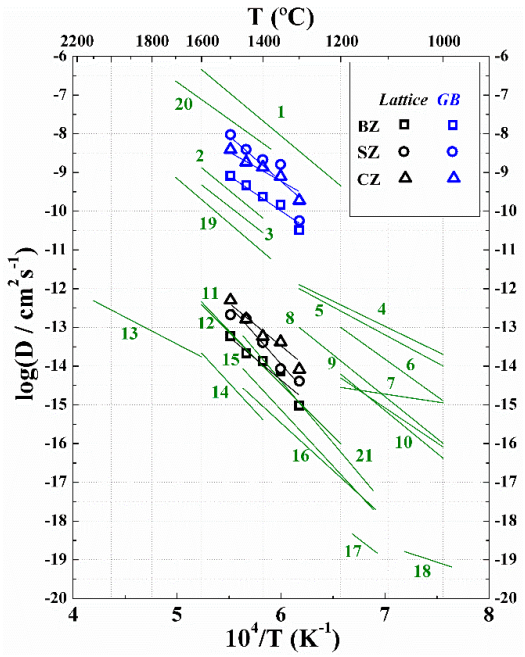

Figure 7. Zr diffusivity in $AZrO_3$ compared to data diffusion data in fluorites. Abbreviations: p—polycrystalline; sc—single crystal; c—cubic; t—tetragonal; b—bulk; gb—grain boundaries. (1) ^{96}Zr in c-ScSZ gb [36]; (2) Yb in t-YSZ gb [49]; (3) Hf in t-YSZ gb [49]; (4) Fe in $(Gd,Ce)O_2$ [50]; (5) Co in $(Gd,Ce)O_2$ [50]; (6) La in $(La,Ce)O_2$ [50]; (7) Co in $(La,Ce)O_2$ [50]; (8) Sr in $(Gd,Ce)O_2$ [51]; (9) Sr in $(Gd,Ce)O_2$ [52]; (10) La in $(Gd,Ce)O_2$ [52]; (11) Yb in t-YSZ b [49]; (12) ^{96}Zr in c-ScSZ b [36]; (13) ^{230}Th in ThO_2 [53]; (14) Hf in t-YSZ b [49]; (15) ^{96}Zr in c-CSZ sc [54]; (6) ^{96}Zr in c-YSZ sc [54]; (17) Gd in CeO_2 gb [55]; (18) Gd in CeO_2 b [55]; (19) ^{88}Y in c-YSZ b [54]; (20) ^{88}Y in c-YSZ gb [54]; (21) ^{44}Ca in c-CSZ [54].

4. Materials and Methods

4.1. Sample Preparation

Dense BZ ceramics were sintered from fine and homogeneous spray-pyrolyzed powders (CerPoTech AS, Trondheim, Norway) at 1600 °C for 10 h in air within sacrificial powder consisting of BZ and 10 wt % $BaCO_3$. The pre-consolidation, consolidation, and sintering procedures of the BZ ceramics have been described previously [8]. Fine CZ powder (Sigma-Aldrich Norway AS, Oslo, Norway) was pressed into pellets by uniaxial pressing with subsequent cold isostatic press (200 MPa), and sintered at 1550 °C for 2 h in air with the heating rate of 700 °C/h. SZ powder was synthesized by solid state reaction using $SrCO_3$ (supplier name) and nanosized ZrO_2 powder (Sigma-Aldrich). The precursors were mixed for 8 h by ball milling with YSZ balls and isopropanol, dried (150 °C), ground, and sieved (150 µm). The synthesis was performed at 1200 °C for 5 h in air. The SZ powder was milled and pressed to pellets, and dense ceramics of SZ were prepared by sintering at 1600 °C for 10 h in air, with a heating rate of 700 °C/h.

The surface of the sintered pellets of the three different ceramics was polished by SiC papers and diamond suspension (down to $\frac{1}{4}$ µm grade) to obtain a flat and smooth surface. The pellets were

pre-annealed at 900 °C for 8 h in synthetic air to clean the surfaces and remove any possible traces of carbonates and water.

The detailed procedure for the deposition of the $^{96}ZrO_2$ films has been reported previously [17]. $^{96}ZrO_2$ with enrichment higher than 85% (Trace Sciences International, Canada) was first transformed to $^{96}ZrO(NO_3)_2{\cdot}xH_2O$, which was dissolved in deionized water (0.05 M), and the solution was drop casted on $AZrO_3$ pellets at 90 °C. The coated pellets were dried at 150 °C. The $^{96}ZrO(NO_3)_2{\cdot}xH_2O$ layer was decomposed at 800 °C for 3 h in flowing N_2, resulting in a dense and homogeneous layer of $^{96}ZrO_2$ (~1–2 μm).

The pellets with the films containing the ^{96}Zr tracer were subjected to diffusion annealing temperatures in the range 1300–1500 °C. The annealing time varied in the range 2–90 h. The conditions for the diffusion anneal was estimated for five samples of each material regarding a constant penetration depth, $x = \sqrt{2Dt} = const$, where D is the diffusion coefficient dependent on temperature and t is time, s.

The phase purity and microstructure of the materials and the tracer layer were characterized by X-ray powder diffraction (XRD) (Bruker, Billerica, MA, USA) and scanning electron microscopy (SEM) (Hitachi, Chiyoda, Tokyo, Japan). The unit cell parameters for the three materials were obtained by Rietveld refinement using previous reported structural models for the three materials [28,56]. The grain size of the materials was evaluated by linear intercept method, from 50 to 60 grains from the SEM images. The chemical composition of the materials was confirmed by energy dispersive X-ray spectroscopy (EDS) (Oxford Instruments, Abingdon, Oxfordshire, UK).

4.2. Secondary Ion Mass Spectrometry

The distribution of the isotopes ^{90}Zr and ^{96}Zr in the ceramics was measured by SIMS using a Cameca IMS 4f instrument (Cameca SAS, Gennevilliers CEDEX, France). The experimental conditions and optimization are given elsewhere [17]. The secondary molecular $^{90}ZrO^-$, and $^{96}ZrO^-$ ion signals were measured as a function of the sputter time. The intensities of the diffusing tracers were collected until the natural abundance of the tracer isotope was approached. The noise in the raw depth profiles was observed only at low intensity levels, which confirmed stable experimental conditions and good charge compensation. The final depth profiles of the isotope tracer were normalized by subtraction of the isotopic ratio of natural abundance [57], in order to avoid instrumental variations. The crater depth was measured with a 3D Laser Scanning Confocal Microscope KEYENCE VK-X100 (KEYENCE, Osaka, Japan). The craters exhibited no considerable roughness at the bottom.

The lattice diffusion coefficient was calculated from the first part of the depth profile (not including the region of the tracer layer with constant concentration) by fitting the experimental data to a solution of the Fick's second law in a case of a thin film source, Equation (5) [20,35]:

$$-\frac{\partial \ln[^{z}M_{norm}]}{\partial x^2} = -\frac{1}{4D_L t} \quad (5)$$

where, D_L is lattice diffusion coefficient ($cm^2{\cdot}s^{-1}$) of isotope ^{z}M with normalized concentration $[^{z}M_{norm}]$ in depth x (cm) at an appropriate time t (s).

Grain boundary transport occurred in the Harrison B-type kinetic regime, where the condition $\delta < \sqrt{Dt} < d$ *or* $1 < d/\sqrt{Dt}$ is fulfilled [20], where d is the average grain size and δ is the grain boundary width. The grain boundary diffusion coefficients were estimated from the part of the depth profiles at deeper sputter depth using the Whipple–Le Clair's equation [20,24]:

$$s\delta D_{GB} = 1.322\sqrt{\frac{D_{eff}}{t}}\left(-\frac{\partial \ln[^{z}M_{norm}]}{\partial x^{6/5}}\right)^{-5/3} \quad (6)$$

where, s is a segregation factor, δ is grain boundary width (cm), D_{GB} is grain boundary diffusion coefficient ($cm^2{\cdot}s^{-1}$), D_{eff} is an effective diffusion coefficient ($cm^2{\cdot}s^{-1}$), and t is annealing time (s).

The effective diffusion coefficient, D_{eff}, represents a combined lattice and grain boundary diffusivity, calculated by, $D_{eff} = gD_{GB} + D_L$, where $g = 3\delta/d$.

5. Conclusions

The lattice and grain boundary diffusion of Zr^{4+} in polycrystalline $AZrO_3$ (A = Ca, Sr, Ba) was determined by ^{96}Zr tracer diffusion experiments. The activation energies for Zr^{4+} lattice diffusion were shown to be 435 ± 67, 505 ± 56, and 445 ± 45 and kJ·mol^{-1}, respectively for $BaZrO_3$, $SrZrO_3$, and $CaZrO_3$. It was suggested that lattice diffusion of Zr^{4+} occurs via A- and B-vacancies based on the previously reported agreement between experiments and calculations in case of $BaZrO_3$. Enhanced diffusivity along grain boundaries was observed for Zr^{4+} in $BaZrO_3$, $SrZrO_3$, and $CaZrO_3$, with activation energies of 356 ± 40, 523 ± 134, and 322 ± 46 kJ·mol^{-1}, respectively. The pre-exponential factor in the Arrhenius expression for diffusion and the activation entropy of diffusion were shown to depend on the unit cell volume per formula unit in a similar manner as the activation enthalpy. The B-site lattice diffusivities for $AZrO_3$ perovskites were lower than in $A^{II}B^{IV}O_3$, and most $A^{III}B^{III}O_3$ perovskites, and in the same range as most fluorite-type oxides. The low Zr^{4+} diffusivity makes the materials robust with respect to B-site mobility in electrochemical potential gradients.

Supplementary Materials: The following are available online at www.mdpi.com/2304-6740/6/1/14/s1, Figure S1: XRD results for sintered $CaZrO_3$ (CZ), $SrZrO_3$ (SZ) and $BaZrO_3$ (BZ) materials, Table S1: Summary of the sintering results and Rietveld refinement of the ceramics.

Acknowledgments: Financial support from NIMS—International Cooperative Graduate Program and The Research Council of Norway under the program NANO2021 to the project (Number 228355) "Functional oxides for clean energy technologies: fuel cells, gas separation membranes and electrolyzers" (FOXCET) conducted by SINTEF Materials and Chemistry, University of Oslo and The Norwegian University of Science and Technology (NTNU) in Trondheim, is gratefully acknowledged.

Author Contributions: Rokas Sažinas performed all the experiments. Tor Grande supervised the work. Isao Sakaguchi supervised the SIMS experiments. Mari-Ann Einarsrud gave valuable advices. Rokas Sažinas and Tor Grande wrote the paper.

Conflicts of Interest: The authors declare no conflict of interest.

References

1. De Souza, E.C.C.; Muccillo, R. Properties and applications of perovskite proton conductors. *Mater. Res.* **2010**, *13*, 385–394. [CrossRef]
2. Phair, J.W.; Badwal, S.P.S. Materials for separation membranes in hydrogen and oxygen production and future power generation. *Sci. Technol. Adv. Mater.* **2016**, *7*, 792–805. [CrossRef]
3. Malavasi, L.; Fisher, C.A.; Islam, M.S. Oxide-ion and proton conducting electrolyte materials for clean energy applications: Structural and mechanistic features. *Chem. Soc. Rev.* **2010**, *39*, 4370–4387. [CrossRef] [PubMed]
4. Kochetova, N.; Animitsa, I.; Medvedev, D.; Demin, A.; Tsiakaras, P. Recent activity in the development of proton-conducting oxides for high-temperature applications. *RSC Adv.* **2016**, *6*, 73222–73268. [CrossRef]
5. Kreuer, K.D. Proton-Conducting Oxides. *Ann. Rev. Mater. Res.* **2003**, *33*, 333–359. [CrossRef]
6. Kreuer, K.D. Aspects of the formation and mobility of protonic charge carriers and the stability of perovskite-type oxides. *Solid State Ion.* **1997**, *125*, 285–302. [CrossRef]
7. Hibino, T.; Mizutani, K.; Yajima, T.; Iwahara, H. Evaluation of proton conductivity in $SrCeO_3$, $BaCeO_3$, $CaZrO_3$ and $SrZrO_3$ by temperature programmed desorption method. *Solid State Ion.* **1992**, *57*, 303–306. [CrossRef]
8. Sažinas, R.; Bernuy-López, C.; Einarsrud, M.-A.; Grande, T. Effect of CO_2 exposure on the chemical stability and mechanical properties of $BaZrO_3$-ceramics. *J. Am. Ceram. Soc.* **2016**, *99*, 3685–3695. [CrossRef]
9. Bera, J.; Rout, S.K. On the formation mechanism of $BaTiO_3$–$BaZrO_3$ solid solution through solid-oxide reaction. *Mater. Lett.* **2005**, *59*, 135–138. [CrossRef]
10. Itoh, J.-I.; Yashima, I.; Ohashi, N.; Sakaguchi, I.; Haneda, H.; Tanaka, J. Ni ion diffusion in barium titanate perovskite. *J. Ceram. Soc. Jpn.* **2001**, *109*, 955–959. [CrossRef]

11. Itoh, J.-I.; Haneda, H.; Hishita, S.; Sakaguchi, I.; Ohashi, N.; Park, D.-C.; Yashima, I. Diffusion and solubility of holmium ions in barium titanate ceramics. *J. Mater. Res.* **2004**, *19*, 3512–3520. [CrossRef]
12. Koerfer, S.; De Souza, R.A.; Yoo, H.-I.; Martin, M. Diffusion of Sr and Zr in $BaTiO_3$ single crystals. *Solid State Sci.* **2008**, *10*, 725–734. [CrossRef]
13. Yoo, H.-I.; Lee, C.-E.; De Souza, R.A.; Martin, M. Equal mobility of constituent cations in $BaTiO_3$. *Appl. Phys. Lett.* **2008**, *92*, 252103. [CrossRef]
14. Lewis, G.V.; Catlow, C.R.A. Computer modelling of barium titanate. *Radiat. Eff.* **1983**, *73*, 307–314. [CrossRef]
15. Mizoguchi, T.; Takahashi, N.; Lee, H.-S. First-principles study on migration mechanism in $SrTiO_3$. *Appl. Phys. Lett.* **2011**, *98*, 091909. [CrossRef]
16. Gömann, K.; Borchardt, G.; Schulz, M.; Gömann, A.; Maus-Friedrichs, W.; Lesage, B.; Kaïtasov, O.; Hoffmann-Eifert, S.; Schneller, T. Sr diffusion in undoped and La-doped $SrTiO_3$ single crystals under oxidizing conditions. *Phys. Chem. Chem. Phys.* **2005**, *7*, 2053–2060. [CrossRef] [PubMed]
17. Sažinas, R.; Sakaguchi, I.; Hasle, I.; Polfus, J.M.; Haugsrud, R.; Einarsrud, M.-A.; Grande, T. Tracer diffusion of ^{96}Zr and ^{134}Ba in polycrystalline $BaZrO_3$. *Phys. Chem. Chem. Phys.* **2017**, *19*, 21878–21886. [CrossRef] [PubMed]
18. Sažinas, R.; Sakaguchi, I.; Einarsrud, M.-A.; Grande, T. ^{134}Ba tracer diffusion in polycrystalline $BaMO_3$ (M = Ti, Zr, Ce). *AIP Adv.* **2017**, *7*, 115024. [CrossRef]
19. Martin, M. Materials in thermodynamic potential gradients. *J. Chem. Thermodyn.* **2003**, *35*, 1291–1308. [CrossRef]
20. Kharton, V.V. *Solid State Electrochemistry II*, 1st ed.; Wiley-VCH: Weinheim, Germany, 2011.
21. Yamanaka, S.; Fujikane, M.; Hamaguchi, T.; Muta, H.; Oyama, T.; Matsuda, T.; Kobayashi, S.-I.; Kurosaki, K. Thermophysical properties of $BaZrO_3$ and $BaCeO_3$. *J. Alloys Compd.* **2003**, *359*, 109–113. [CrossRef]
22. Yamanaka, S.; Kurosaki, K.; Oyama, T.; Muta, H.; Uno, M.; Matsuda, T.; Kobayashi, S.-I. Thermophysical properties of perovskite-type strontium cerate and zirconate. *J. Am. Ceram. Soc.* **2005**, *88*, 1496–1499. [CrossRef]
23. Szczerba, J.; Pdzich, Z.; Madej, D. Synthesis of spinel-calcium zirconate materials. *Mater. Ceram.* **2011**, *63*, 27–33.
24. Gryaznov, D.; Fleig, J.; Maier, J. An improved procedure for determining grain boundary diffusion coefficients from averaged concentration profiles. *J. Appl. Phys.* **2008**, *103*, 063717. [CrossRef]
25. Gömann, K.; Borchardt, G.; Gunhold, A.; Maus-Friedrichs, W.; Baumann, H. Ti diffusion in La-doped $SrTiO_3$ single crystals. *Phys. Chem. Chem. Phys.* **2004**, *6*, 3639–3644. [CrossRef]
26. Kennedy, B.J.; Howard, C.J.; Chakoumakos, B.C. High-temperature phase transitions in $SrZrO_3$. *Phys. Rev. B* **1999**, *59*, 4023–4027. [CrossRef]
27. Wang, K.; Li, C.H.; Gao, Y.H.; Lu, X.G.; Ding, W.Z. Thermodynamic reassessment of ZrO_2–CaO System. *J. Am. Ceram. Soc.* **2009**, *92*, 1098–1104. [CrossRef]
28. Mathews, M.D.; Mirza, E.B.; Momin, A.C. High-temperature X-ray diffractometric studies of $CaZrO_3$, $SrZrO_3$ and $BaZrO_3$. *J. Mater. Sci. Lett.* **1991**, *10*, 305–306. [CrossRef]
29. Grande, T.; Tolchard, J.R.; Selbach, S.M. Anisotropic thermal and chemical expansion in Sr-substituted $LaMnO_{3+\delta}$: Implications for chemical strain relaxation. *Chem. Mater.* **2012**, *24*, 338–345. [CrossRef]
30. Stokes, S.J.; Islam, M.S. Defect chemistry and proton-dopant association in $BaZrO_3$ and $BaPrO_3$. *J. Mater. Chem.* **2010**, *20*, 6258–6264. [CrossRef]
31. Klyukin, K.; Alexandrov, V. Effect of intrinsic point defects on ferroelectric polarization behavior of $SrTiO_3$. *Phys. Rev. B* **2017**, *95*, 035301. [CrossRef]
32. Davies, R.A.; Islam, M.S.; Gale, J.D. Dopant and proton incorporation in perovskite-type zirconates. *Solid State Ion.* **1999**, *126*, 323–335. [CrossRef]
33. Yamazaki, Y.; Yang, C.-K.; Haile, S.M. Unraveling the defect chemistry and proton uptake of yttrium-doped barium zirconate. *Scr. Mater.* **2011**, *65*, 102–106. [CrossRef]
34. Shannon, R.D. Revised effective ionic radii and systematic studies of interatomic distances in halides and chalcogenides. *Acta Cryst. A* **1976**, *32*, 751–767. [CrossRef]
35. Crank, J. *The Mathematics of Diffusion*; Oxford University Press: Oxford, UK, 1975.
36. Taylor, M.A.; Kilo, M.; Borchardt, G.; Weber, S.; Scherrer, H. ^{96}Zr diffusion in polycrystalline scandia stabilized zirconia. *J. Eur. Ceram. Soc.* **2005**, *25*, 1591–1595. [CrossRef]

37. Dobson, T.W.; Wager, J.F.; Van Vechten, J.A. Entropy of migration for atomic hopping. *Phys. Rev. B* **1989**, *40*, 2962–2967. [CrossRef]
38. Smith, D.W. An acidity scale for binary oxides. *J. Chem. Educ.* **1987**, *64*, 480–481. [CrossRef]
39. Xu, J.; Yamazaki, D.; Katsura, T.; Wu, X.; Remmert, P.; Yurimoto, H.; Chakraborty, S. Silicon and magnesium diffusion in a single crystal of $MgSiO_3$ perovskite. *J. Geophys. Res.* **2011**, *116*, 1–8. [CrossRef]
40. Palcut, M.; Christensen, J.S.; Wiik, K.; Grande, T. Impurity diffusion of ^{141}Pr in $LaMnO_3$, $LaCoO_3$ and $LaFeO_3$ material. *Phys. Chem. Chem. Phys.* **2008**, *10*, 6544–6552. [CrossRef] [PubMed]
41. Palcut, M.; Wiik, K.; Grande, T. Cation self-diffusion in $LaCoO_3$ and La_2CoO_4 studied by diffusion couple experiments. *J. Phys. Chem. B* **2007**, *111*, 2299–2308. [CrossRef] [PubMed]
42. Miyoshi, S.; Martin, M. B-Site cation diffusivity of Mn and Cr in perovskite-type $LaMnO_3$ with cation-deficit nonstoichiometry. *Phys. Chem. Chem. Phys.* **2009**, *11*, 3063–3070. [CrossRef] [PubMed]
43. Palcut, M.; Knibbe, R.; Wiik, K.; Grande, T. Cation inter-diffusion between $LaMnO_3$ and $LaCoO_3$ materials. *Solid State Ion.* **2011**, *202*, 6–13. [CrossRef]
44. Petrov, A.N.; Rabinovich, L.Y.; Zhukovskii, V.M.; Zhukovskaia, A.S. Diffusion of the metallic components in sintered lanthanoid orthocobaltites $LnCoO_3$ (Ln = La, Pr, Nd, Sm, Eu, Gd). *Dokl. Chem.* **1987**, *292*, 18–21.
45. Sakai, N.; Yamaji, K.; Horita, T.; Negishi, H.; Yokokawa, H. Chromium diffusion in lanthanum chromites. *Solid State Ion.* **2000**, *135*, 469–474. [CrossRef]
46. Smith, J.; Norby, T. Cation self-diffusion in $LaFeO_3$ measured by the solid state reaction method. *Solid State Ion.* **2006**, *177*, 639–646. [CrossRef]
47. Pavlyuchenko, M.M.; Filonov, B.O.; Shimanovich, I.E.; Produkina, S.A. Fe diffusion in $NdFeO_3$. *Dokl. Akad. Nauk BSSR* **1970**, *14*, 328–350.
48. Kishimoto, H.; Sakai, N.; Horita, T.; Yamaji, K.; Brito, M.; Yokokawa, H. Cation transport behavior in SOFC cathode materials of $La_{0.8}Sr_{0.2}CoO_3$ and $La_{0.8}Sr_{0.2}FeO_3$ with perovskite structure. *Solid State Ion.* **2007**, *178*, 1317–1325. [CrossRef]
49. Swaroop, S.; Kilo, M.; Argirusis, C.; Borchardt, G.; Chokshi, A.H. Lattice and grain boundary diffusion of cations in 3YTZ analyzed using SIMS. *Acta Mater.* **2005**, *53*, 4975–4985. [CrossRef]
50. Sakai, N.; Kishimoto, H.; Yamaji, K.; Horita, T.; Brito, M.E.; Yokokawa, H. Interface stability of perovskite cathodes and rare-earth. Doped ceria interlayer in SOFCs. *J. Electrochem. Soc.* **2007**, *154*, B1331–B1337. [CrossRef]
51. Chen, P.-L.; Chen, I.W. Role of defect interaction in boundary mobility and cation diffusivity of CeO_2. *J. Am. Ceram. Soc.* **1994**, *77*, 2289–2297. [CrossRef]
52. Izuki, M.; Brito, M.E.; Yamaji, K.; Kishimoto, H.; Cho, D.-H.; Shimonosono, T.; Horita, T.; Yokokawa, H. Interfacial stability and cation diffusion across the LSCF/GDC interface. *J. Power Sources* **2011**, *196*, 7232–7236. [CrossRef]
53. Freer, R. Self-diffusion and impurity diffusion in oxides. *J. Mater. Sci.* **1980**, *15*, 803–824. [CrossRef]
54. Kilo, M.; Taylor, M.A.; Argirusis, C.; Borchardt, G.; Lesage, B.; Weber, S.; Scherrer, S.; Scherrer, H.; Schroeder, M.; Martin, M. Lanthanide transport in stabilized zirconias: Interrelation between ionic radius and diffusion coefficient. *J. Appl. Phys.* **2003**, *94*, 7547–7552. [CrossRef]
55. Rockenhäuser, C.; Butz, B.; Schichtel, N.; Janek, J.; Oberacker, R.; Hoffmann, M.J.; Gerthsen, D. Microstructure evolution and cation interdiffusion in thin Gd_2O_3 films on CeO_2 substrates. *J. Eur. Ceram. Soc.* **2014**, *34*, 1235–1242. [CrossRef]
56. Tarrida, M.; Larguem, H.; Madon, M. Structural investigations of $(Ca,Sr)ZrO_3$ and $Ca(Sn,Zr)O_3$ perovskite compounds. *Phys. Chem. Miner.* **2009**, *36*, 403–413. [CrossRef]
57. Vocke, R.D. Atomic weights of the elements 1997. *Pure Appl. Chem.* **1999**, *71*, 1593–1607. [CrossRef]